Anomalous electronic properties in layered, disordered ZnVSb

Erik A. Bensen,[1] Kamil Ciesielski,[1,2,*] Lídia C. Gomes,[3,4] Brenden R. Ortiz,[1,5] Johannes Falke,[6] Orest Pavlosiuk,[2] Daniel Weber,[7] Tara L. Braden,[1] Kenneth X. Steirer,[1] Damian Szymański,[2] Joshua E. Goldberger,[7] Chang-Yang Kuo,[6,8] Chien-Te Chen,[8] Chun-Fu Chang,[6] Liu Hao Tjeng,[6] Dariusz Kaczorowski,[2] Elif Ertekin,[3] and Eric S. Toberer[1,†]

[1]*Physics Department, Colorado School of Mines, Golden, Colorado 80401, USA*
[2]*Institute of Low Temperature and Structure Research, Polish Academy of Sciences, 50-422 Wrocław, Poland*
[3]*University of Illinois at Urbana-Champaign, Urbana, Illinois 61820, USA*
[4]*Instituto de Física Teórica, São Paulo State University (UNESP), São Paulo 01049-010, Brazil*
[5]*University of California Santa Barbara, Santa Barbara, California 93106-9010, USA*
[6]*Max Planck Institute for Chemical Physics of Solids, 01187 Dresden, Germany*
[7]*Department of Chemistry and Biochemistry, The Ohio State University, Columbus, Ohio 43210, USA*
[8]*National Synchrotron Radiation Research Center (NSRRC), 30076 Hsinchu, Taiwan*

(Received 22 August 2020; revised 23 November 2020; accepted 22 December 2020; published 27 January 2021)

New materials discovery is the driving force for progress in solid state physics and chemistry. Here we solve the crystal structure and comprehensively study physical properties of ZnVSb in the polycrystalline form. Synchrotron x-ray diffraction reveals that the compound attains a layered ZrSiS-type structure ($P4/nmm$, $a = 4.09021(2)$ Å, $c = 6.42027(4)$ Å). The unit cell is composed of a 2D vanadium network separated by Zn-Sb blocks that are slightly distorted from the ideal cubic arrangement. A considerable amount of vacancies were observed on the vanadium and antimony positions; the experimental composition is $ZnV_{0.91}Sb_{0.96}$. Low-temperature x-ray diffraction shows very subtle discontinuity in the lattice parameters around 175 K. Bonding V-V distance is below the critical separation of 2.97 Å known from the literature, which allows for V-V orbital overlap and subsequent metallic conductivity. From *ab initio* calculations, we found that ZnVSb is a pseudogap material with an expected dominant vanadium contribution to the density of states at the Fermi level. The energy difference between the antiferromagnetic and nonordered magnetic configurations is rather small (0.34 eV/f.u.). X-ray photoelectron spectroscopy fully corroborates the results of the band structure calculations. Magnetic susceptibility uncovered that, in ZnVSb, itinerant charge carriers coexist with a small, localized magnetic moment of ca. 0.25 μ_B. The itinerant electrons arise from the ordered part of the vanadium lattice. Fractional localization, in turn, was attributed to V atoms neighboring vacancies, which hinder full V-V orbital overlap. Furthermore, the susceptibility and electrical resistivity showed a large hysteresis between 120 K and 160 K. The effect is not sensitive to magnetic fields up to 9 T. Curie-Weiss fitting revealed that the amount of itinerant charge carriers in ZnVSb drops with decreasing temperature below 160 K, which is accompanied by a concurrent rise in the localized magnetic moment. This observation together with the overall shape of the hysteresis in the resistivity allows for suggesting a plausible origin of the effect as a charge-transfer metal-insulator transition. *Ab initio* phonon calculations show the formation of a collective phonon mode at 2.8 THz (134 K). The experimental heat capacity reflected this feature by a boson peak with Einstein temperature of 116 K. Analysis of the heat capacity with both an *ab initio* perspective and Debye-Einstein model revealed a sizable anharmonic contribution to heat capacity, in line with disordered nature of the material. Further investigation of the electron and phonon properties for ZnVSb is likely to provide valuable insight into the relation between structural disorder and the physical properties of transition-metal-bearing compounds.

DOI: 10.1103/PhysRevMaterials.5.015002

I. INTRODUCTION

The discovery of new pnictides with intriguing properties has been a key driver within solid state chemistry [1–6]. Among thermoelectric pnictide materials, binaries such as Zn_4Sb_3 [1] and Mg_3Sb_2 [2] as well as more complex compounds, e.g., $Yb_{14}MnSb_{11}$ [3], have exhibited excellent performance. Likewise, layered pnictide superconductors have emerged, such as those based on LiFeAs [4], $BaFe_2As_2$ [5], and LaOFeAs [6]. This rich space for functional properties to emerge is created by combinations of the structural complexity afforded by Zintl-like pnictide bonding, moderate electronegativity contrast, and transition metals with un-paired spins. In this work, we extend this investigation to the polar intermetallic pnictide ZnVSb.

ZnVSb has previously emerged in the context of galvanizing steel metallurgical chemistry [7]. Polycrystalline

*k.ciesielski@intibs.pl
†etoberer@mines.edu

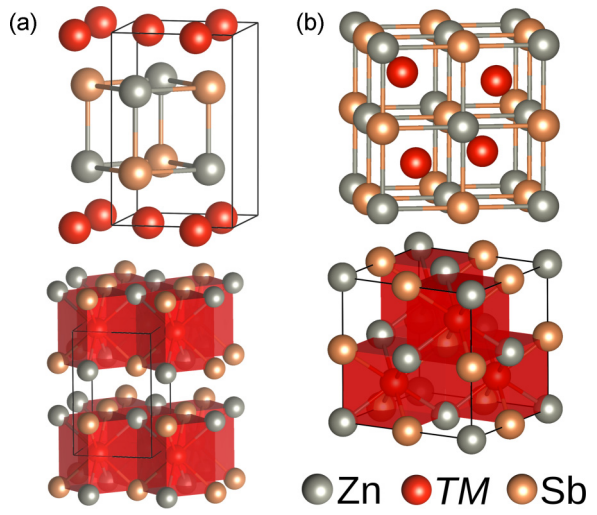

FIG. 1. Ternary compounds containing transition metals with Zn and Sb tend to form in either the (a) ZrSiS or (b) half-Heusler structure types. Here Zn is in gray, Sb in orange, and the transition metal (TM) in red. Below the eightfold coordination polyhedra around the transition metals are highlighted.

specimens were prepared by melt synthesis followed by annealing and quenching. The chemical composition, identified by energy-dispersive x-ray analysis, was found to span in range 30.4–32.4 at.%V, 30.5–34.0 at.%Zn, and 34.7–37.1 at.%Sb. ZnVSb was found to share three-phase regions with various combinations of V_3Sb, ZnSb, Zn_4Sb_3, Zn_3Sb_2, and elemental Zn. Isothermal phase diagram studies at elevated temperature (450 °C [7], 600°C [8]) find that ZnVSb is the only ternary compound present in the Zn-V-Sb space. The phase disappears by 800 °C [8].

To date, the crystal structure of ZnVSb has not been identified. Known ternary zinc antimonides include ZnMnSb [9], ZnFeSb [10,11], ZnCoSb [12], and ZnNiSb [13], $Zn_9In_2Sb_6$ [14], $ZnSnSb_2$ [15], and $Zn_5In_2Sb_4$ [16]. Within the transition metal-containing ternary zinc antimonides, all existing compounds possess equimolar stoichiometry and form in either the ZrSiS or half-Heusler-like structure types. The ZrSiS model is sometimes used interchangeably with PbFCl, UAs_2, and Cu_2Sb due to the same space group and occupied Wyckoff sites. In the literature, however, one can find several attempts to demarcate these structure types due to a variety of chemical bonding [17–19]. The ZrSiS model was chosen for ZnVSb as the closest ternary prototype.

As shown in Fig. 1(a), there is a $-[A_2 - B - C - C - B]-$ layer repeat pattern in the ZrSiS model. Key structural features include (1) the z offset between the B and C planes, which can give rise to a skew of the rock salt-like slab, and (2) significant variability in anion and cation site preference due to variations in size and charge. Both the half-Heusler [Fig. 1(b)] and ZrSiS-type antimonides have eightfold coordinated transition metals but the arrangement of these polyhedra is distinct.

ZnMnSb has been reported to form in the ZrSiS structure type; this compound exhibits ferromagnetic ordering with a T_C of 302 K [9]. ZnMnSb also exhibits nearly temperature-independent resistivity of 5 mΩcm below T_C, which was attributed to intense point defect scattering due to structural disorder. In the original report the authors suggested ZnMnSb may have ∼5% and ∼10% vacancies for the Zn and Mn sites, respectively, or a strong tendency towards cation alloying. ZnFeSb was initially reported as a half-Heusler compound [10]; however, more recently it has been shown that it will adopt a half-Heusler-like supercell with cation-deficient composition when annealed at 570 K or the ZrSiS structure type when heated to 873 K with closer to a stoichiometric atomic ratio [11]. Low temperature measurements of ZnFeSb in the ZrSiS structure reveal a nearly temperature-independent resistivity of 14 mΩcm and a ferromagnetic ordering temperature of 275 K. Akin to ZnFeSb, ZnCoSb forms in a superstructure of the half-Heusler phase. The resistivity is distinctly lower, 0.2 mΩcm, and no long-range magnetic ordering is observed [12]. The compound ZnNiSb has been reported to form in the cubic MgAgAs (Half-Heusler) structure type. Its resistivity follows metallic behavior and attains a value of 0.039 mΩcm at room temperature [20].

In the present study of ZnVSb, we develop a synthetic procedure and determine the resulting crystal structure. The low temperature electrical, phononic, and magnetic properties are then explored in light of crystallographic disorder and first principles calculations. We find that ZnVSb encompasses itinerant and localized electrons, most likely originating from the ordered and disordered components of the vanadium sublattice. Furthermore, between 120 K and 160 K we detect a unique phenomenon of a charge-transfer metal-insulator transition affecting a fraction of V atoms without full orbital overlap due to disorder.

II. METHODS

A. Experimental methods

Samples of ZnVSb were synthesized from elemental reagents: Zn (flake, Alfa 99.9%), V (granules, Alfa 99.7%), and Sb (shot, Alfa 99.999%). All sample preparation and handling of powders was performed in a nitrogen glove box (oxygen <3 ppm, water <1 ppm). Elemental reagents were sealed into tungsten carbide vials and ball milled for 90 min in a Spex 8000D high-energy ball mill.

For structure determination, undoped, as-milled powders were sealed into fused silica ampules and annealed at 600 °C for 48 h under vacuum. Resulting powders were ground in an agate mortar and passed through a 50 μm mesh. Then, all samples were diluted with amorphous silica powder at a molar ratio of 1:2 powder:silica to reduce x-ray absorption. Diluted powders were sealed within polyimide (Kapton) capillaries and measured at the Advanced Photon Source (APS) beamline 11-BM. Low-temperature measurements were conducted on a PANalytical Empyrean diffractometer from 90 K to 300 K. The crystal structure was solved by means of Pawley refinement and charge flipping in Topas Academic V6 software, while the main Rietveld refinement was performed in the FullProf package [21] for ease of comparison with large amount of literature data. Rietveld analysis with Topas Academic V6 is provided in the Supplemental Material (SM) Fig. S1 and Table S1 [22].

For electronic transport measurements, annealed powders were densified through hot-pressing in a high-density graphite

die under dynamic vacuum. Prior to use, the graphite die, plungers, and graphite foil liners were baked at 600 °C for a minimum of 30 min under dynamic vacuum. Approximately 1.75 g of annealed powder was loaded into the cooled die and transferred to the hot press chamber. The chamber was evacuated to <5 mTorr and purged with argon to ∼0.75 Atm thrice before finally evacuating the chamber to <1 mTorr. The powder was pressed at 50 MPa and 550 °C for 12 h.

X-ray energy dispersive imaging was performed utilizing a FEI NovaNanoSEM 230 FE-scanning electron microscope employed with a Genesis XM4 spectrometer. Magnetic susceptibility and magnetization experiments were performed on a Quantum Desing MPMS-XL magnetometer with a solid specimen cut from the densified pellet. Electrical resistivity and specific heat measurements were performed on the Quantum Desing PPMS-9 platform. The pellets were cut into rectangular shapes and contacted in a linear, four-point probe geometry via silver paste and silver wires with 50 μm diameter. For the specific heat the relaxation method with the two-τ model was employed, the experiment at the lowest temperatures was performed with the ^{3}He option.

X-ray photoelectron spectroscopy (XPS) and x-ray absorption spectroscopy (XAS) experiments were performed at the NSRRC-MPI TPS 45A Submicron Soft X-ray Spectroscopy beamline at the Taiwan Photon Source in Taiwan. The photoemission chamber is equipped with an MB Scientific A-1 electron energy analyzer and operates in ultra-high vacuum with a pressure of 1×10^{-10} mbar. The photon energy was set to $h\nu = 1010$ eV, and the overall energy resolution was $\approx$100 meV as determined from the Fermi cutoff of a gold reference sample.

B. Computational methods

Electronic band structure calculations were performed within density functional theory (DFT) [23,24] implemented in the Vienna Ab initio Simulation Package (VASP) [25]. The generalized gradient approximation (GGA) of Perdew-Burke-Ernzerhof (PBE) [26] and the projector augmented wave formalism [27] were used. The Kohn-Sham orbitals were expanded using a plane-wave basis with a cutoff energy of 400 eV. Lattice parameters and atomic positions were fully relaxed until forces were lower than 1 meV/Å on each atom. The Brillouin zone was sampled using a Γ-centered $8 \times 8 \times 4$ Monkhorst-Pack k-point grid [28]. Total and partial density of states were computed using a finer Γ-centered grid of $30 \times 30 \times 28$ k points and plotted using the Sumo Python toolkit [29]. For the calculations including magnetism, the DFT + U approach was used, as proposed by Dudarev *et al.* [30]. The additional Hubbard-like term was used to treat the on-site Coulomb interactions on the localized d orbitals of vanadium and zinc atoms. In this case, a finer k-mesh grid of $16 \times 16 \times 12$ was employed.

To obtain the phonon dispersions of ZnVSb, VASP was used in conjunction with the Phonopy package [31], based on the supercell approach with the finite displacement method [32]. A very strict structural optimization of the lattice parameters and atomic positions was performed, with convergence criteria of 10^{-2} meV/Å. As in the electronic band structure calculation, we added the Hubbard-like term to the d orbitals of vanadium atoms. Phonopy was used to determine the force constants, the phonon dispersions, and the phonon projected density of states using $2 \times 2 \times 2$ supercells and a $4 \times 4 \times 3$ k-point mesh.

III. RESULTS AND DISCUSSION

A. Structure refinement

The results from powder diffraction measurements were analyzed using Pawley refinement and revealed that ZnVSb crystallizes in the $P4/nmm$ space group. Subsequent charge flipping identified the compound forms in a layered ZrSiS-type structure. Figure 2(a) presents the Rietveld refinement of the synchrotron powder diffraction data. Structural data and technical details are shown in Table I, while atomic coordinates, occupancies, and displacement parameters, as well as selected interatomic distances, are gathered in Table II. The atomic occupancy on each site was relaxed initially as a separate free parameter and eventually the results were normalized to Zn content.

The structure of ZnVSb, provided in Fig. 1(a), can be viewed as rock-salt slabs of ZnSb separated by a square 2D net of V. Each Zn and Sb atom is coordinated by four V atoms from this monolayer. However, the corrugation of the rock-salt slab yields slightly different (<1%) V-Sb and V-Zn bond distances (Table II). This nearly cubic Zn-Sb bonding arrangement is quite unusual compared to the typical bonding arrangements for Zn-Sb [1,33], Zn-V [34,35] or V-Sb [36–40] binary compounds. However, the bond angles and interatomic distances of the rock salt-like ZnSb slabs are consistent with chemically similar ZrSiS-type compounds, e.g., ZnMnSb [9], ZnFeSb [11], AlMnGe [41], and GaMnGe [42]. For magnetism and electrical properties, the most important interatomic distance for ZnVSb is V-V bond length, which is equal to 2.892 Å. This distance is smaller than the critical V-V separation known from literature, $R_C = 2.97$ Å. The value of R_C marks the border between itinerant (V-V distance $< R_C$) or localized (V-V distance $> R_C$) behavior predicted for vanadium d electrons due to orbital overlap [43,44].

Figure 2(b) shows laboratory XRD data collected in the 90–300 K regime. ZnVSb maintains its structure type from 300 K down to 90 K. No clear indication of atomic rearrangement such as a superstructure peak nor a change of relative maxima intensities were observed. Lattice parameters (a and c) obtained by Rietveld refinement performed for scans at each temperature are presented in Fig. 2(c). Between 150 K and 175 K one can notice small discontinuity in a and c on the very edge of the accuracy of the method. Benefiting from an almost linear variation of elementary cell volume with temperature, we calculated the thermal expansion coefficient for ZnVSb, $\alpha = 14.2 \times 10^{-6}$ K^{-1}, which is broadly consistent with values found for metals and metallic alloys [45].

Concerning the stoichiometry of the ZnVSb phase, x-ray refinement assuming vacancies suggests that the composition of the main phase is depleted in V and to smaller extent also in Sb; such refinement yields $ZnV_{0.91}Sb_{0.96}$ (see Table II). Alternatively, Rietveld refinement can be performed assuming the possibility of antisite defects, which, after checking all combinations, leads to a small amount of Zn-Sb intermixing.

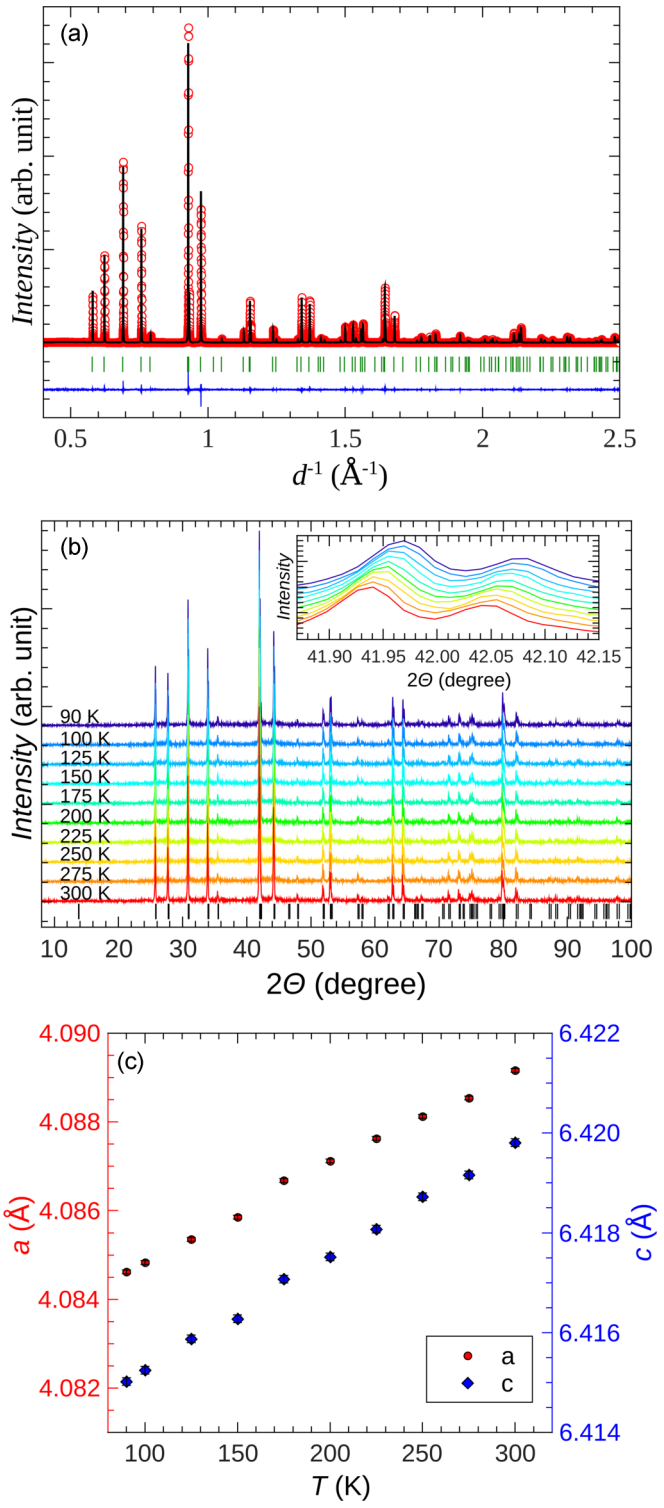

FIG. 2. (a) X-ray diffraction pattern from 11-BM beamline on ZnVSb powder (red) and Rietveld fit (black) using the ZrSiS structure type; the difference pattern is shown in blue. (b) Laboratory powder x-ray diffraction collected across 90–300 K. Inset shows the temperature-dependence of the (112) reflection from $K_{\alpha 1}$ and $K_{\alpha 2}$ radiation. (c) Rietveld refinement of the patterns presented in (b) yield linear changes in lattice parameters.

The occupancies in this model would be Zn 97.31(7)% + Sb 2.69(5)% on nominal zinc site, 92.1(1)% vanadium occupancy on its unchanged Wyckoff position and Sb 95.41(7) % + Zn 3.5(1) % on the nominal antimony site. In either case, the stoichiometry is depleted slightly in V and Sb. These results are consistent with EDX measurements, which found that ZnVSb is depleted in vanadium by ca. 10 at.%. The ZnVSb phase diagram at 450 °C indicates adjoining phases are Zn, Zn_3Sb_2, Zn_4Sb_3, ZnSb, and V_3Sb [7]; however, we do not observe any signal from those compounds in the synchrotron powder XRD.

TABLE I. Structural and technical information on analysis of synchrotron powder diffraction data for ZnVSb.

Composition	$ZnV_{0.91}Sb_{0.96}$
Structure type	ZrSiS
Space group	$P4/nmm$, no. 129
Pearson symbol, Z	$tP6$-δ, 2
a (Å)	4.09021(2)
c (Å)	6.42027(4)
V (Å^3)	107.410(1)
Density (g/cm^3)	7.06(2)
No. of Bragg maxima observed	327
No. of refined parameters	16
Radiation wavelength (Å)	0.412602
Temperature of measurement	300 K
R_{wp}	11.4
G.O.F.	2.07

B. Electronic structure

To investigate the electronic and magnetic properties, we performed first-principles DFT calculations of the electronic band structure and density of states. Hubbard-like onsite Coulomb potential U was applied to the V and Zn 3d orbitals due to their localized nature. As the optimal value of U cannot be determined *a priori*, we performed calculations with $U = 0$, +3, and +5 eV for vanadium and $U = +5$, +6, and +7 eV for zinc, typical values used in the literature [46–49], and compared the results.

For all U values, it was determined that ZnVSb exhibits a metallic character with no gap around the Fermi energy. Figure 3 shows the electronic band structure of ZnVSb, plotted here for the intermediate values $U = +3$ eV and +6 eV for vanadium and zinc, respectively, for the non spin-polarized case. In the vicinity of the Fermi level (E_F, shifted here to 0 eV), there are many bands with relatively low dispersion. The flat character of these bands is more evident just above the E_F (along X-M-Γ, R-A, X-R, and M-A) as well as for some filled bands, in particular along Γ-Z.

The projected DOS in Fig. 3(b) shows that the states in the range ~ -2 to 4 eV around the E_F are formed mostly from the vanadium 3d orbitals. This can be seen in more detail in the fat bands plot shown in the SM (Fig. S2). The metallic nature can be attributed to the partial filling of the overlapping V 3d orbitals. The 3d levels of Zn, on the other hand, are fully occupied and located at much lower energies (∼10 eV below the E_F). A minor contribution to the states around the E_F is also observed from the Zn and Sb orbitals. Within 1 eV from the E_F, the main contribution from these atoms is to the band

TABLE II. Atomic positions, displacement coefficients, and occupancies as well as selected interatomic distances in ZnVSb from Rietveld refinement of synchrotron powder diffraction data.

Atom	Wyckoff site	x	y	z	B_{iso}	Occupancy
Zn	2c	1/4	1/4	0.2826(6)	1.02(7)	1
V	2a	1/4	3/4	0	0.52(8)	0.906(2)
Sb	2c	1/4	1/4	0.7099(4)	0.53(3)	0.959(1)
	d (Å)		d (Å)		d (Å)	
Zn-Sb vertical	2.723	Zn-V	2.747	V-V 1st	2.892	
Zn-Sb horizontal	2.892	Sb-V	2.767	V-V 2nd	4.090	

with parabolic dispersion around Γ, originating from Sb and Zn s orbitals. Sb p orbitals form the more dispersive filled bands from ∼1 eV below the E_F. Interestingly, just above the E_F the density of states decreases rapidly to almost zero in a semimetallic manner, which also can be described as a pseudogap; see Fig. 3(c). This feature will be referred to during the analysis of electrical resistivity.

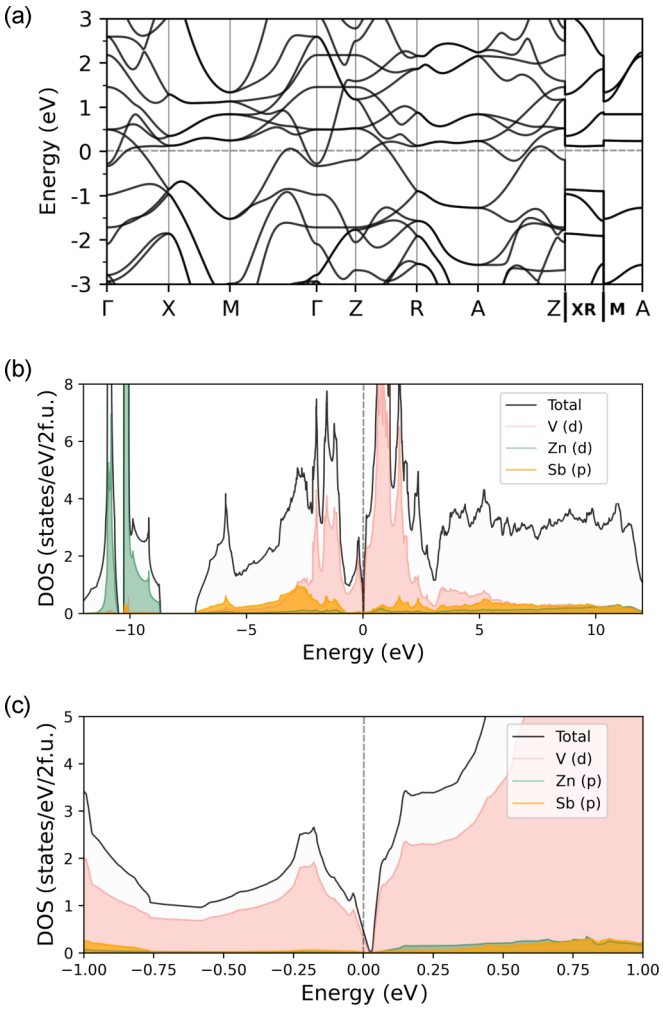

FIG. 3. Electronic structure of ZnVSb calculated using the Hubbard corrections $U = +3$ eV and $+6$ eV for vanadium and zinc d orbitals, respectively. (a) Electronic band structure of ZnVSb shows a metallic ground state with the appearance of several flat, dispersionless states around the Fermi level. (b) The projected density of states shows that the states around the Fermi level are mostly derived from the V 3d orbitals. Exchange splitting of the 3d orbitals above and below the Fermi level results in the dip in the total DOS at $E_F = 0$ eV, as shown in detail at the zoomed region in (c).

Calculations including spin polarization were also performed to investigate the formation of magnetic moments and impact on the electronic properties. The atomic orbital contributions to the electronic band structure are essentially the same as in the non-spin-polarized case. For more details of spin-polarized calculations the reader is referred to Fig. S3 in the SM.

C. Magnetism and electronic transport properties

Figure 4(a) shows the magnetic susceptibility (χ) of ZnVSb. The general curvature of χ is reminiscent of paramagnetic behavior, yet between 120 K and 160 K, the susceptibility exhibits a significant thermal hysteresis [see inset to Fig. 4(a)], which might be associated with a first-order phase transition. The effect occurs intact at the same temperatures during measurements in magnetic field up to 7 T (not shown). To get better insight into underlying physics of ZnVSb, the susceptibility was analyzed via

$$\chi(T) = \frac{C}{T - \Theta_p} + \chi_0, \tag{1}$$

where Θ_p corresponds to the paramagnetic Curie temperature, χ_0 stands for temperature independent susceptibility, and $C = \mu_{\text{eff}}^2/8$ and μ_{eff} denotes the effective magnetic moment. The parameter χ_0 corresponds to Pauli-like paramagnetism, and the term $\frac{C}{T-\Theta_p}$ describes Curie-Weiss localized magnetism. Regions above and below hysteresis were treated separately: the red solid curve corresponds to fit performed in 2–120 K range, while the blue solid curve denotes analysis for 170–300 K range. The dashed lines serve only as a guide to the eye—they extend calculated functions beyond fitting range. Parameters obtained from the analysis are gathered in Table III.

The coexistence of itinerant and localized magnetism, assumed by Eq. (1) for ZnVSb, was previously observed for other vanadium-based compound [50–52]. Both effects are associated with V ions, yet in different crystallographic environment. In ZnVSb itinerant magnetism is likely a feature of the majority of the vanadium atoms with regular arrangement, while localized magnetism may be associated with a small part of the V ions experiencing a modified surrounding due to disorder. The above understanding is built upon the values

TABLE III. Parameters resultant from least-squares fitting of Eq. (1) to susceptibility data [see Fig. 4(a)].

	LT fit (2–100 K)	HT fit (170–300 K)
μ_{eff} (μ_B)	0.262(3)	0.239(2)
Θ_p (K)	−6.5(2)	−3.4(2)
χ_0 (10^{-4} emu mol^{-1} Oe^1)	1.21(4)	1.89(2)

of parameters obtained from Eq. (1). The effective magnetic moments equal to ca. 0.25 μ_B are rather small for vanadium. In the states V^{2+}, V^{3+}, and V^{4+} the ion exhibits μ_{eff} equal to 3.87, 2.83, and 1.73μ_B, respectively. Significant reduction of μ_{eff} in ZnVSb with respect to theoretical values suggests that localized moments are present for only a fraction of the V atoms. These can be atoms for which full V-V orbital overlap is not present due to vacancies on V site.

Reduced μ_{eff} on vanadium atoms has previously been observed, e.g., for V_5S_8 comprising itinerant and localized magnetic behavior. In V_5S_8, 1/5 vanadium atoms were expected to possess localized moments [50]. The particular ratio was due to the proportion of multiplicity of two different Wyckoff sites on which V atoms resided. Regarding the Pauli paramagnetic behavior of the matrix, the sizable value of χ_0 supports the possibility that a rather large fraction of the sample (matrix) is related to this phenomenon.

Regardless of the value of the Hubbard correction chosen for Zn and V during spin-polarized calculations, the energy difference between the ordered and nonordered magnetic states is fairly small (0.34 eV/f.u.; see details in the SM). This finding suggests that ZnVSb can easily change its magnetic behavior, which qualitatively supports the possibility of localized moment formation at a fraction of V atoms experiencing disorder. The antiferromagnetic spin alignment was most energetically favorable in *ab initio* calculations, which is in agreement with negative Θ_p from Eq. (1) indicating antiferromagnetic fluctuations.

Compared to the susceptibility near room temperature, the value of χ_0 becomes smaller below 170 K, suggesting that the density of delocalized states decreases with decreasing temperature. In turn, the magnetic moment and paramagnetic Curie temperature rise simultaneously, which indicate that the number of localized V atoms increase below 170 K. Together these results allow for tentative interpretation of the hysteresis as a sign of a partial charge-transfer (CT) metal-insulator transition (MIT). For the further consideration of the effect the reader is referred to Sec. F below.

The magnetization isotherms [Fig. 4(b); collected at 2, 5, 10, 80, 140 K) show a Brillouin-like shape, reminiscent of paramagnetic materials, however, the lack of saturation in $\sigma(T)$ even at the highest fields hindered fitting the data with a classical Brillouin function. Deviations from pure Brillouin behavior in magnetization were previously observed, e.g., for diluted magnetic alloys or semiconductors due to the exchange interaction between magnetic ions [53,54], or the interplay of Kondo effect and RKKY interactions [55,56] These systems are somewhat similar to ZnVSb, which shows only small fraction of V with magnetic moment in their Pauli paramagnetic matrix. Attempting to systematically change the

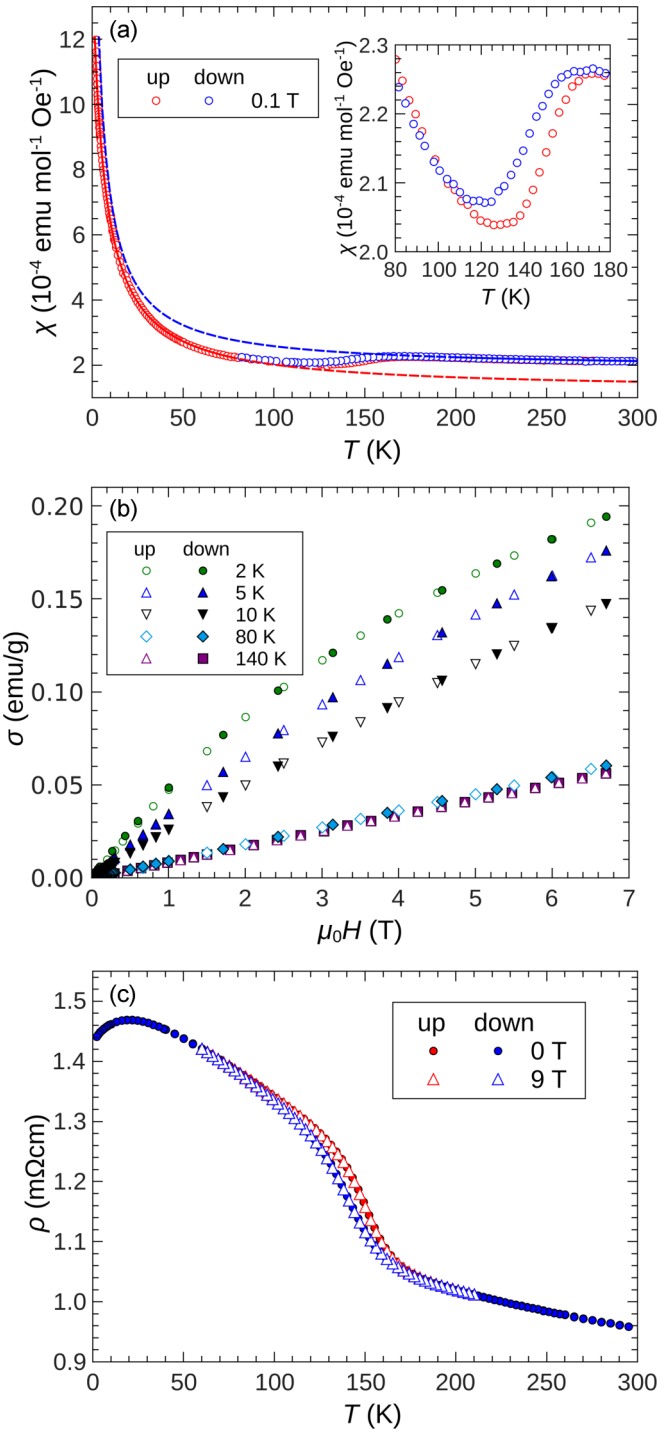

FIG. 4. (a) Temperature variation of magnetic susceptibility for ZnVSb in the field of 0.1 T. Red and blue symbols correspond to increasing and decreasing temperature, respectively. Solid curves denote fits of Eq. (1), while dashed lines extend the obtained function beyond fitting range as guide to the eye. The inset displays susceptibility measurement in the regime of thermal hysteresis. (b) Field dependencies of magnetization measured at temperatures 2 K, 5 K, 10 K, 80 K, and 140 K. Empty and filled symbols denote increasing and decreasing field, respectively. (c) Temperature dependence of electrical resistivity for ZnVSb measured in the field of 0 T (filled symbols) and 9 T (open symbols). Red and blue denote measurements performed with increasing and decreasing temperature, respectively.

percentage of magnetic vanadium atoms in the material, e.g., by altering the nominal composition ($ZnV_{1-x}Sb$) or modifying the synthesis route appears as a fascinating topic for further studies aimed at the precise description of magnetic interactions in ZnVSb. The lack of dependence on magnetic history of the sample, corroborates the paramagnetic state of the studied compound. We note that magnetization measurements were performed well below and well above the onset of thermal hysteresis.

The electrical resistivity (ρ) of ZnVSb is displayed in Fig. 4(c). The relatively small value of 0.96 mΩcm at room temperature is in line with the predictions from crystal structure analysis, which suggested metallic behavior due to V-V orbitals overlap. This finding is also consistent with band structure calculations showing a small, yet finite density of states at Fermi level. As expected, V provides the dominant component of the pDOS at E_F. However, the temperature behavior of ρ is not as expected for typical metallic systems, i.e., the resistivity of ZnVSb does not rise with increasing temperature due to phonon scattering. We rather observe a slight decrease of ρ with rising temperature, also referred as a negative temperature coefficient of resistivity (TCR $= \frac{1}{\rho}\frac{d\rho}{dT}$). This feature is commonly observed in semimetals [57,58], metals with significant disorder in the crystal lattice [59,60], and/or large grain boundary resistance [61,62]. For example, negative thermal coefficients of resistivities have been reported in NbN thin films [62] and Ti-Ni alloys [60]. Moreover, the absolute values of ρ change rather weakly with temperature, from 1.44 mΩcm at 2 K to 0.96 mΩcm at 300 K. The small variation of ρ with T suggests that point defect scattering with rather weak temperature dependence might be an important scattering source for ZnVSb. Also the kink in the density of states near E_F [see Fig. 3(c)] might be partially responsible for this nontrivial curvature of ρ. Furthermore, to rule out the possibilities of technical factors related to polycrystalline nature of the sample influencing its resistivity, single crystal growth of ZnVSb is necessary. In the 120–160 K regime, we observe a slight thermal hysteresis in resistivity, which corresponds to observation of very similar effect in $\chi(T)$ [see Fig. 4(a)]. Assuming that the effect in ρ also originates from CT MIT, we might understand the increase of resistivity as a result of fractional localization of carriers in ZnVSb with decreasing temperature below 170 K. The phenomenon in $\rho(T)$ is not sensitive to a magnetic field, which is shown by open triangles in Fig. 4(c) denoting experiment performed with $\mu_0 H = 9$ T.

D. Photoelectron spectroscopy

A wide energy range spectrum is presented in Fig. 5(a) and confirms that the investigated ZnVSb specimen contains only the expected elements. All features, including the Sb MMN Auger lines as shown in the inset of Fig. 5(a), can be identified. Figure 5(b) displays the Sb 3d and V 2p core levels. The positions of the most prominent peaks for vanadium are the $2p_{3/2}$ at 512.1 eV and the $2p_{1/2}$ at 520.3 eV binding energies. These locations are in agreement with the metallic state of V [63]. Insulating V compounds have their V 2p core levels at higher binding energies [64–66]. We have also carried out x-ray absorption experiments across the V $L_{2,3}$ edges of ZnVSb (see Fig. S4) and have observed rather featureless white

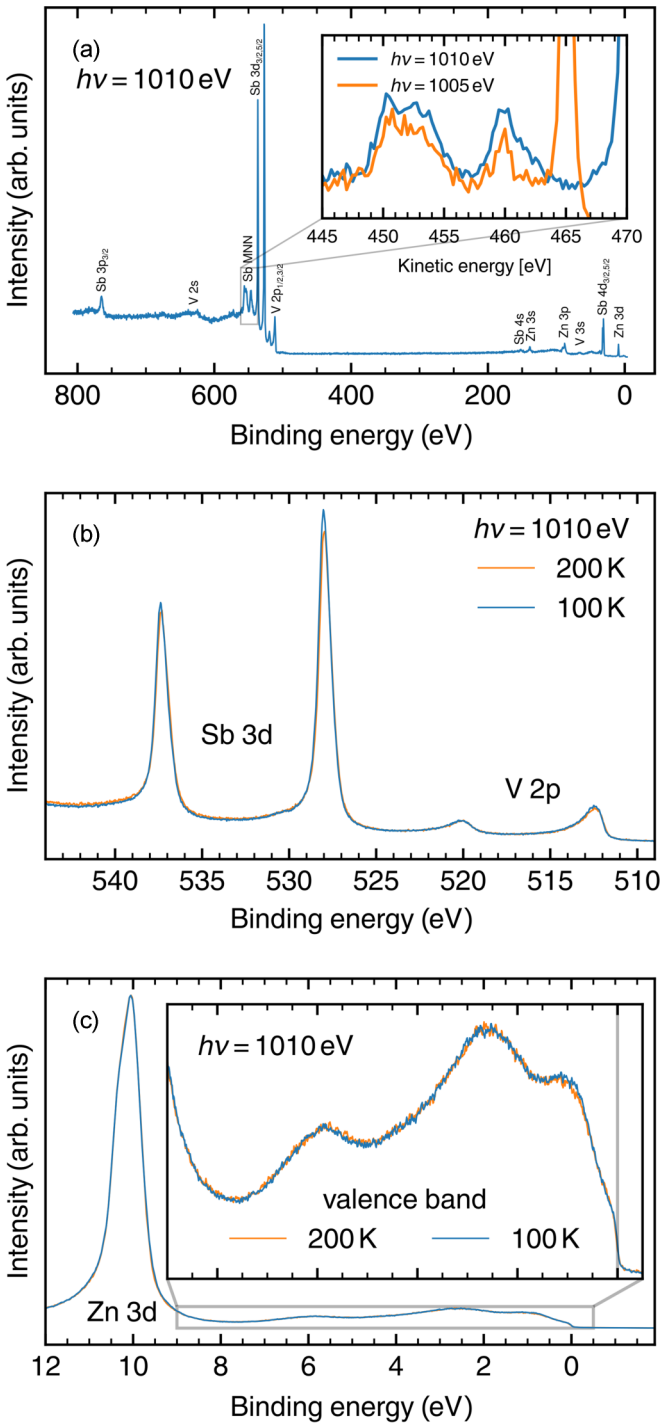

FIG. 5. XPS data of ZnVSb taken at 100 K (blue lines) and 200 K (orange lines): (a) wide energy range scan with the inset displaying the Sb MNN Auger lines; (b) the Sb 3d and V 2p core levels; (c) the extended valence band with the inset showing an enlarged view on the valence band.

lines, very different from the spectra of insulating V compounds which show pronounced multiplet structures [67–70]. This again points to a metallic state of V. All these observations are consistent with the understanding of the ZnVSb crystal structure (V-V overlapping orbitals), *ab initio* calculations and electrical resistivity. Also the predictions of Pauli

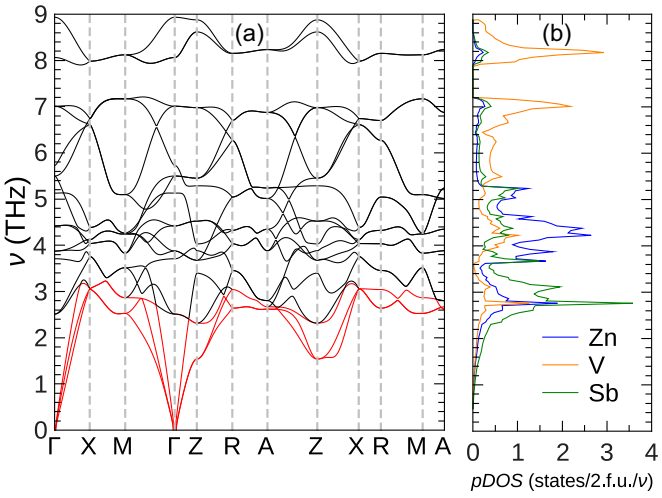

FIG. 6. (a) Phonon dispersion relation for ZnVSb, red and black lines correspond to acoustic and optical branches, respectively. (b) Related partial phonon density of states.

paramagnetic behavior for the majority of ZnVSb sample are in agreement with a bulk metallic state of V.

The valence band spectrum is presented in Fig. 5(c). The three humps visible between 0 eV and 7 eV nicely correspond to the DOS maxima obtained by *ab initio* calculations in this energy regime (cf. Fig. 3). Also the Zn 3*d* peak located at 10 eV binding energy in the experiment is reproduced by the DFT calculations.

We have performed the above-mentioned XPS and XAS experiments at 100 K and 200 K, as indicated by the blue and orange lines, respectively. No significant changes can be observed. There is only a slight increase in peak width, which can be attributed to temperature broadening.

E. Heat capacity

The phonon dispersion relation along representative high-symmetry lines is displayed in Fig. 6(a). These results were obtained applying the same values of the Hubbard corrections as in the electronic structure calculations, i.e., $U = +3$ eV and $+6$ eV for vanadium and zinc d orbitals, respectively. Six atoms in the unit cell of ZnVSb lead to three acoustic and 15 optical branches, which are shown by red and black lines, respectively. Lack of modes with the negative frequency confirms stability of the crystal structure; no evidence of rattling or other anomalies are present. The associated phonon partial density of states is shown in Fig. 6(b). As expected, the main contributions of the respective elements are located at frequencies inversely related to the atomic masses, i.e., the heaviest antimony ($A = 51$) contributed dominantly to low-lying modes at around 3 THz, the Zn ($A = 30$) peak is centered at 4.4 THz and the main modes from vanadium ($A = 22$) are distributed between at 7 and 8.2 THz. Around 2.8 THz, the density of states forms a narrow peak, which will be referred to in heat capacity analysis.

The experimental heat capacity (C_p) of ZnVSb is displayed on linear and logarithmic scales in Fig. 7 and Fig. S5, respectively. The overall temperature dependence of $C_p(T)$ attains a classical sigmoid-like shape. Near room temperature, the C_p values are close to the Dulong-Petit harmonic approximation of $3k_B$ per atom (74.8 $\mathrm{Jmol^{-1}K^{-1}}$; using moles of formula unit), shown by the dashed line in Fig. 7. No phase transition is observed in the experimental data; the small hump near 170 K is a technical feature resultant from the changed step between data points [see inset to Fig. 7(a)].

The theoretical phononic contribution to C_p was obtained by numerically integrating the *ab initio* phonon density of states over frequency in order to get the total energy (U):

$$U = \int_0^{\nu_{\max}} \mathrm{DOS}(\nu) f(\nu, T) \left(h\nu + \frac{1}{2} \right) d\nu, \tag{2}$$

where $\mathrm{DOS}(\nu)$ corresponds to the total phonon density of states, $f(\nu, T)$ denotes the Fermi-Dirac distribution function, and ν stands for the frequency. To calculate the heat capacity we then take the temperature derivative of the total energy: $C_{ph} = \frac{\delta U}{\delta T}$. The result shown as the blue line in Fig. 7(a) is close to the experimental data up to 150 K, with only gentle overestimation of C_p values in range 70–110 K, which might be ascribed to numerical uncertainties in phonon density of states and/or inaccuracy of the C_p experiment. Above 150 K, the *ab initio* phonon heat capacity is considerably lower than the observed one, which will be addressed in further analysis, including electronic contribution and ahnarmonicity.

The electronic contribution to C_p was approximated using three approaches: (1) Sommerfeld model with fitted parameters to low temperature C_p, (2) Sommerfeld model from *ab initio* DOS, and (3) a more complete analysis utilizing the full density of states. In the first approach, the heat capacity data were fitted in the range 3–8 K with the formula

$$\frac{C_P}{T} = \gamma + \beta T^2 + \eta T^4, \tag{3}$$

where the Debye relevant for low temperatures is $\Theta_D^* = \sqrt[3]{\frac{12\pi^4}{\beta}} nR = 314$ K, and η stands for the higher order term in the power series approximation of the Debye integral (for details see, e.g., Ref. [71]). This approach yielded γ value of 7.4 $\mathrm{mJ\,mol^{-1}\,K^{-2}}$; see Fig. 7(b). The parameter η is a small correction to β, its value is $1.6(2) \times 10^{-8}$ $\mathrm{J\,mol^{-1}\,K^{-6}}$. Interestingly, below 3 K C_p/T forms considerable upturn. The effect is strengthened after application of magnetic field equal to 0.5 T and 1 T [blue and red circles in Fig. 7(b)]. Our tentative interpretation of the phenomenon's origin is the Zeeman effect visible already without external magnetic field, due to nonzero internal field distribution in our sample. The source for this internal field is probably the fraction of vanadium atoms with noncomplete d-electron overlap due vacancies on the V site. Splitting of energy levels should result in a Schottky anomaly in heat capacity. Sensitivity of the effect on external magnetic field is reminiscent of observations for systems with two or more energy levels [72,73]. Confirmation of this preliminary hypothesis requires further studies in higher magnetic fields and preferentially on single crystalline specimens, which is planned as a follow-up study. Alternative interpretations of this upturn in C_p/T might be spin fluctuations. This phenomenon, however, is expected to be destroyed by the magnetic field, which is not observed for ZnVSb. Lastly, we thought of a contribution from nuclear heat

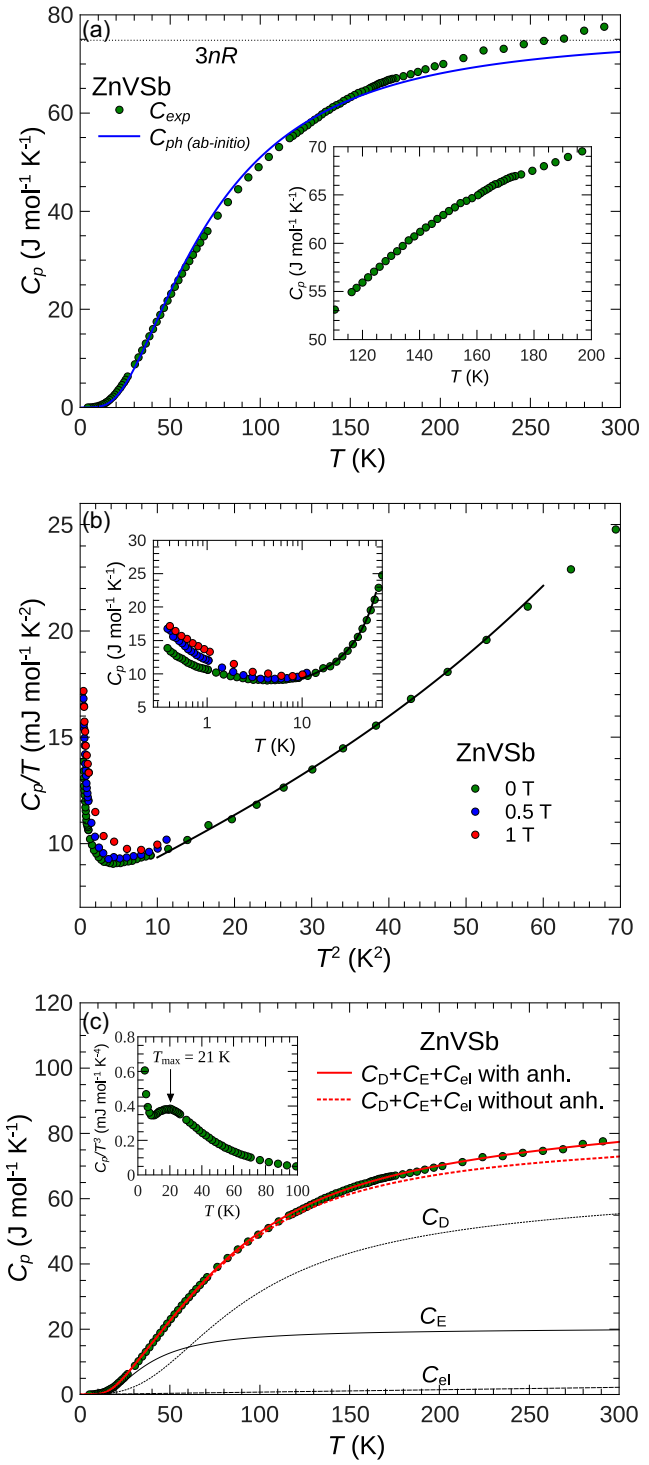

FIG. 7. Temperature dependence of the specific heat for ZnVSb. (a) Experimental data compared to lattice contribution calculated from *ab initio* phonon density of states (blue line); see text for the details. Inset displays the temperature regime investigated with smaller step between data points. (b) The low-temperature data in C_p/T vs T^2 representation. Solid line is Debye fit; see text. Inset shows the data in the logarithmic axis x for better visualization of the very lowest temperatures. (c) Analysis of the capacity with the Debye-Einstein model corrected for anharmonicity. The Debye, Einstein, and electronic contributions are displayed with black dotted, solid, and dashed lines, respectively. Inset shows data in C_p/T^3 vs T representation.

capacity, yet the temperature of upturn (2 K) appears to be too high for such an effect.

The second approach to electronic heat capacity based on the density of states $N(E_F) = 0.47$ states/eV/2.f.u. at E_F, utilizes the parabolic band approximation: $\gamma_{ab\,initio} = 1/3\pi^2 k_B^2 N(E_F)$. From this approach, a Sommerfeld coefficient of 0.58 mJ mol^{-1} K^{-2} is obtained. Enhancement of the observed γ with respect to theoretical expectations is often ascribed to the electron-electron interactions that are not taken into account during *ab initio* work [74–76] or in special cases to disorder-related phenomena [77–80].

Lastly, the electronic heat capacity can be calculated from the density of states under the presumption of a temperature-independent electronic structure. The first step is to determine the temperature-dependence of the chemical potential μ, as it will shift with temperature due to nonconstant density of states near E_F. This is achieved by calculating the total electrons up to E_F at 0 K, and then iteratively determining μ to conserve the total electron count (n) at each temperature step,

$$n = \int g(E) f(E)\, dE, \tag{4}$$

where $g(E)$ and $f(E)$ are the *ab initio* density of states and Fermi-Dirac distribution function. With $E_F(T)$ determined, the second step is then to determine the total energy

$$U = \int E f(E) g(E)\, dE \tag{5}$$

for each temperature step. Finally, a numerical derivative in temperature is then taken between these points to determine the electronic heat capacity. This approach yields electronic contribution to heat capacity at 300 K of 0.54 J mol^{-1} K^{-2}. The reader is referred to Fig. (S6) in the SM for the temperature dependence of the so-obtained electronic heat capacity.

Summing the electronic and phononic heat capacities leaves a significant residual at room temperature, regardless of which method outlined above is employed. To make up this discrepancy, in linear approximation of C_p a γ value of $\sim$22 mJ mol^{-1} K^{-2} would be required; instead, the simpler explanation is that anharmonic effects alter the phononic heat capacity with temperature. The effect might plausibly originate from paramagnetic magnons due to localized V atoms, or disorder in the crystal structure [81], i.e., a certain number of dangling bonds due to vacancies on V and Sb sites. Also, large amount of vacancies in ZnVSb might change the harmonic phonon spectrum of the compound.

In Fig. 7(c) we show further heat capacity analysis with Debye-Einstein model corrected for anharmonicity [82]

$$C_p(T) = \gamma T + (1-w)\frac{C_D(T)}{1-\alpha_D T} + w\frac{C_E(T)}{1-\alpha_E T}, \tag{6}$$

$$C_D = 9nR\left(\frac{T}{\Theta_D}\right)^3 \int_0^{\Theta_D/T} \frac{x^4 \exp(x)}{[\exp(x)-1]^2}\, dx, \tag{7}$$

$$C_E = 3nR\left(\frac{\Theta_E}{T}\right)^2 \left[\exp\left(\frac{\Theta_E}{T}\right) - 1\right]^{-2} \exp\left(\frac{\Theta_E}{T}\right), \tag{8}$$

where γ stands for the Sommerfeld coefficient, Θ_D and Θ_E denote Debye and Einstein temperatures, respectively, w corresponds to weight coefficient, while α_D and α_E are anharmonicity factors for Debye and Einstein modes, respectively. The Sommerfeld coefficient was fixed during the analysis to the previously derived value of 7.4 mJ mol^{-1} K^{-2}. Least-square fitting of Eq. (6) well reproduced heat capacity in the whole temperature investigated. The obtained parameters are $\Theta_D = 367(2)$ K, $\Theta_E = 116(1)$ K, $w = 0.26(1)$, $\alpha_D = 2.37(4)\times10^{-4}$ K^{-1}, and $\alpha_E = 1.00(9)\times10^{-4}$ K^{-1}.

Despite the roughness of the core assumption in the Debye model [DOS(ν) $\propto \nu^2$], the formula is able to provide qualitatively correct information on the material, including especially the cutoff frequency ω_D in the phonon spectrum. In the case of ZnVSb, experimental Θ_D can be recalculated into $\omega_D = 7.7$ THz. The cutoff frequency derived from *ab initio* phonon dispersion is 8.9 THz (cf. Fig. 6). Bearing in mind a simple assumption of the Debye model and the fact that calculations were performed for the ideal, disorder-free ZnVSb structure, the correspondence between these two results can be considered as satisfactory.

The Einstein model, in turn, assuming common frequency for all vibration modes is more relevant in description of special collective modes in the phonon spectrum, e.g., due to low-frequency rattling [83,84], boson peaks [85,86], or van Hove singularities [87,88]. In the case of ZnVSb, the Einstein contribution to C_p can be easily correlated with the narrow peak localized in projected DOS at 2.8 THz (see Fig. 6). Recalculated to the temperature scale, the maximum locates at 134 K. This value is reasonably close to the result of Eqs. (6)–(8) ($\Theta_E = 116$ K), bearing in mind idealistic treatment of ZnVSb crystal structure during phonon calculations and simplifications of the Einstein model.

We can additionally verify our usage of Einstein model by inspecting the data in representation of C_p/T^3 vs T [inset to Fig. 7(c)]. In concert with expectation, we can see the maximum located at temperature $T_{\max} = 21$ K related to Einstein temperature as $5T_{\max} \approx \Theta_E$. This relation can be easily justified by taking the Eq. (8) in the low-temperature limit [$\exp(\frac{\Theta_E}{T}) \gg 1$]

$$C_E/T^3 = 3nR\frac{\Theta_E^2}{T^5}\left[\exp\left(\frac{\Theta_E}{T}\right)\right]^{-1} \tag{9}$$

and differentiating by the temperature

$$\frac{d(C_E/T^3)}{dT} = 3nR\frac{\Theta_E^2\exp(-\Theta_E/T)(\Theta_E - 5T)}{T^7} = 0 \tag{10}$$

with the solution $T_{\max} = \Theta_E/5$. The phonon properties of ZnVSb, especially the collective Einstein mode can be further inspected by THz spectroscopy. Based on our findings from heat capacity analysis we would expect a peak in absorption near 2.4 THz. The value was obtained from recalculation to terahertz the experimental Einstein temperature $\Theta_D = 116$ K. Somewhat similar studies, including also Raman spectroscopy were performed, e.g., for ZrW_2O_8 and $ZrMo_2O_8$ [89].

Anharmonicity coefficients for Einstein and Debye modes are consistent with the values reported in the literature for intermetallic compounds, the exemplary values are from 1.6 $\times$ 10^{-5} K^{-1} to 6.4 $\times$ 10^{-4} K^{-1} for $ThNi_2Si_2$ [90] or in the 2−7 $\times$ 10^{-5} K^{-1} range for $PrNi_4Si$ [91]. The anharmonic behavior in phonon properties is frequently related to structural disorder [81,92]. In the case of ZnVSb it most likely originates from dangling bonds due to vacancies on vanadium site and to a smaller extent from internal strain due to possible Zn-Sb antisite defects.

F. Discussion

In light of the χ, ρ, C_p, XPS, and LT XRD results presented above, we return to the hysteresis observed around 140 K [see Figs. 4(a) and 4(c)]. The interpretation of this effect as a partial charge-transfer metal-insulator transition appears consistent from the perspective of magnetic susceptibility and electrical resistivity. However, no corresponding signal is detected in heat capacity, or XPS. A plausible resolution to the controversy might be that only a small fraction of charge carriers in ZnVSb are affected by this interesting phenomenon. Such a picture would be in general agreement with understanding of the performed measurements: ρ and χ being very sensitive to the gentle electronic effects, while C_p, and XPS constitute far less sensitive bulk probes. The effect might be also somewhat related with the subtle discontinuity in changes of lattice parameters nearby 175 K; see Fig. 2(b). Further studies preferentially on single crystalline specimens are necessary to gain better understanding of this behavior.

Previously, CT MIT were extensively studied for various transition metal containing systems [93] with special attention to nickel-based perovskites $RNiO_3$ where R denotes the rare-earth metal [94–97]. The driving force for the CT MIT in these compounds is commonly the change of orbital hybridization resultant from a first-order structural phase transition. The modification of physical properties for the literature examples due to CT MIT is more pronounced than in the case of ZnVSb. The resistivity change up to several orders of magnitude and the transition is usually accompanied by an anomaly in heat capacity. Reduced signatures of CT MIT in ZnVSb with respect to the literature is in concert with assumption that only a small fraction of total electrons is affected by the phenomenon.

A fairly good correspondence to observed hither effects in $\rho(T)$ and $\chi(T)$ was found for the nano-sized samples of vanadium oxide V_2O_3 [98,99]. Due to the special nature of these specimens it is not possible to search the driving force of CT MIT in ZnVSb as a direct analog for nano-V_2O_3. However, the fact that recent studies of V_2O_3 show that its MIT originate from a mixture between charge-transfer and Mott-Hubbard types [100,101], might serve as a guide in the future search for the origin of the phenomenon in ZnVSb. As the effect in ZnVSb is probably related to the disorder, studies in which the amount of lattice imperfections is changed intentionally, e.g., by nominal nonstoichiometry or different temperatures of annealing might provide valuable insight on this curious phenomenon.

IV. CONCLUSION

ZnVSb was synthesized and found to crystallize in the ZrSiS-type structure with a significant concentration of vacancies on the V and Sb sites. Low temperature diffraction showed the structure to remain rather stable down to 90 K, apart from a subtle discontinuity in the lattice parameters

between 150 K and 175 K. Electronic structure calculations in line with transport measurements revealed that ZnVSb is a poor metal. The negative thermal coefficient of resistivity combined with its weak temperature dependence indicate that charge transport is predominantly influenced by disordered point defect scattering. Bulk ZnVSb shows Pauli paramagnetic behavior; however, a small localized moment was detected via susceptibility measurement and was ascribed to V atoms without full orbital overlap due to disorder. XPS measurements fully corroborate *ab initio* electron band structure. Phonon dispersion calculations and analysis of experimental heat capacity suggest the presence of anharmonic processes in ZnVSb and a collective phonon mode with Einstein temperature $\Theta_E = 116$ K. The susceptibility and resistivity exhibited a large thermal hysteresis in the 120–160 K range. The origin of this anomaly is most likely a partial charge-transfer metal-insulator transition; however, the driving force of this charge transition remains an intriguing question. Further studies of ZnVSb are likely to contribute to better understanding of the relationship between structural defects and transport properties in transition metal-based compounds.

ACKNOWLEDGMENTS

Use of the Advanced Photon Source at Argonne National Laboratory was supported by the US Department of Energy, Office of Science, Office of Basic Energy Sciences, under Contract No. DE-AC02-06CH11357. E.A.B. and E.S.T. acknowledge support from the National Science Foundation (NSF), Grant No. DMR 1555340. L.C.G. and E.E. gratefully acknowledge support from NSF Grant No. DMR 1729149. L.C.G. also acknowledges the support from the Coordination for the Improvement of Higher Education Personnel (CAPES) Brazilian Agency within the Recruitment of Young Talents with International Experience (JTEE) CAPES/PrInt Program. O.P. was supported by the Foundation for Polish Science (FNP) Program No. START 66.2020. D.W. acknowledges the financing from the German Science Foundation DFG Research Fellowship (Grant No. WE6480/1). J.E.G. acknowledges support from the NSF Grant No. EFRI-1433467. The XPS/XAS measurements in Taiwan were supported by the Max Planck-POSTECH-Hsinchu Center for Complex Phase Materials.

[1] J. Lin, X. Li, G. Qiao, Z. Wang, J. Carrete, Y. Ren, L. Ma, Y. Fei, B. Yang, L. Lei, and J. Li, Unexpected high-temperature stability of β-Zn_4Sb_3 opens the door to enhanced thermoelectric performance, J. Am. Chem. Soc. **136**, 1497 (2014).

[2] C. L. Condron, S. M. Kauzlarich, F. Gascoin, and G. J. Snyder, Thermoelectric properties and microstructure of Mg_3Sb_2, J. Solid State Chem. **179**, 2252 (2006).

[3] S. R. Brown, S. M. Kauzlarich, F. Gascoin, and G. J. Snyder, $Yb_{14}MnSb_{11}$: New high efficiency thermoelectric material for power generation, Chem. Mater. **18**, 1873 (2006).

[4] J. H. Tapp, Z. Tang, B. Lv, K. Sasmal, B. Lorenz, P. C. W. Chu, and A. M. Guloy, LiFeAs: An intrinsic FeAs-based superconductor with $T_C = 18$ K, Phys. Rev. B **78**, 060505(R) (2008).

[5] P. L. Alireza, Y. T. C. Ko, J. Gillett, C. M. Petrone, J. M. Cole, G. G. Lonzarich, and S. E. Sebastian, Superconductivity up to 29 K in $SrFe_2As_2$ and $BaFe_2As_2$ at high pressures, J. Phys.: Condens. Matter. **21**, 012208 (2008).

[6] Y. Kamihara, T. Watanabe, M. Hirano, and H. Hosono, Iron-based layered superconductor $La_{1-x}F_xFeAs$ ($x = 0.05$–0.12) with $T_C = 26$ K, J. Am. Chem. Soc. **130**, 3296 (2008).

[7] Z. Zhu, S. Peng, W. Zhu, Q. Xu, M. Chen, and F. Yin, Experimental investigation of the Zn-V-Sb system at 450 °C, J. Phase Equilib. Diffus. **36**, 120 (2015).

[8] S. Peng, Z. Zhu, W. Ma, Q. Xu, M. Chen, and F. Yin, The 600 °C and 800 °C isothermal sections of the Zn-V-Sb system, Int. J. Mater. Res. **107**, 21 (2016).

[9] V. Johnson and W. Jeitschko, Ferromagnetic anti-PbFCl-type ZnMnSb, J. Solid State Chem. **22**, 71 (1977).

[10] I. Chumak, V. Pavlyuk, G. Dmytriv, and J. Stepień-Damm, Phase equilibria and crystal structure of compounds in the Fe-Zn-Sb system at 570 K, J. Alloys Compd. **307**, 223 (2000).

[11] D.-B. Xiong and Y. Zhao, Half-Heusler phase related structural perturbations near stoichiometric composition FeZnSb, J. Solid State Chem. **184**, 1159 (2011).

[12] D.-B. Xiong, N. L. Okamoto, T. Waki, Y. Zhao, K. Kishida, and H. Inui, High-T_C ferromagnetic semiconductor-like behavior and unusual electrical properties in compounds with a $2 \times 2 \times 2$ superstructure of the half-Heusler phase, Chem.-Eur. J. **18**, 2536 (2012).

[13] I. Chumak and V. Pavlyuk, Interaction of the components in the Ni-Zn-Sb ternary system at 570 K, J. Alloys Compd. **367**, 85 (2004).

[14] Y. Wu, A. Tenga, S. Lidin, and U. Haussermann, Phase relations and structural properties of the ternary narrow gap semiconductors $Zn_5Sb_4In_2$ and $Zn_9Sb_6In_2$, J. Solid State Chem. **183**, 1574 (2010).

[15] A. Nomura, S. Choi, M. Ishimaru, A. Kosuga, T. Chasapis, S. Ohno, G. J. Snyder, Y. Ohishi, H. Muta, S. Yamanaka, and K. Kurosaki, Chalcopyrite $ZnSnSb_2$: A promising thermoelectric material, ACS Appl. Mater. Interf. **10**, 43682 (2018).

[16] Y. Wu, A. P. Litvinchuk, E. S. Toberer, G. J. Snyder, N. Newman, A. Fischer, E.-W. Scheidt, W. Scherer, and U. Haussermann, Thermoelectric properties of $Zn_5Sb_4In_2$, J. Appl. Phys. **111**, 123712 (2012).

[17] J. Flahaut, Les structures type PbFCl (EO_I) et type anti-Fe_2As (C38) des composés ternaires à deux anions MXY, J. Solid State Chem. **9**, 124 (1974).

[18] J. Nuss and M. Jansen, Zur Abgrenzung der PbFCl- und Cu_2Sb-Strukturfamilien: Neubestimmung und Verfeinerung der Kristallstrukturen von CuMgSb, Cu_2Sb und CuMgAs, Z. Anorg. Allg. Chem. **628**, 1152 (2002).

[19] D. O. Charkin and X. N. Zolotova, A crystallographic re-investigation of Cu_2Sb-related binary, ternary, and quaternary structures: How many structure types can exist upon the same topology of a unit cell, Crystallogr. Rev. **13**, 201 (2007).

[20] F. D. Rosi, J. P. Dismukes, and E. F. Hockings, Semiconductor materials for thermoelectric power generation up to 700 °C, Electr. Eng. **79**, 450 (1960).

[21] J. Rodriguez-Carvajal, Recent advances in magnetic structure determination by neutron powder diffraction, Physica B **192**, 55 (1993).

[22] See Supplemental Material at http://link.aps.org/supplemental/10.1103/PhysRevMaterials.5.015002 for further information about Rietveld refinement, fat bands plot from *ab initio* electronic structure calculations, figures from x-ray absorption spectroscopy, and additional electronic heat capacity analysis.

[23] W. Kohn and L. J. Sham, Self-consistent equations including exchange and correlation effects, Phys. Rev. **140**, A1133 (1965).

[24] P. Hohenberg and W. Kohn, Inhomogeneous electron gas, Phys. Rev. **136**, B864 (1964).

[25] G. Kresse and J. Furthmüller, Efficient iterative schemes for *ab initio* total-energy calculations using a plane-wave basis set, Phys. Rev. B **54**, 11169 (1996).

[26] J. P. Perdew, K. Burke, and M. Ernzerhof, Generalized Gradient Approximation Made Simple, Phys. Rev. Lett. **77**, 3865 (1996).

[27] P. E. Blöchl, Projector augmented-wave method, Phys. Rev. B **50**, 17953 (1994).

[28] H. J. Monkhorst and J. D. Pack, Special points for Brillouin-zone integrations, Phys. Rev. B **13**, 5188 (1976).

[29] A. M. Ganose, A. J. Jackson, and D. O. Scanlon, Sumo: Command-line tools for plotting and analysis of periodic *abinitio* calculations, J. Open Source Soft. **3**, 717 (2018).

[30] S. L. Dudarev, G. A. Botton, S. Y. Savrasov, C. J. Humphreys, and A. P. Sutton, Electron-energy-loss spectra and the structural stability of nickel oxide: An LSDA+U study, Phys. Rev. B **57**, 1505 (1998).

[31] A. Togo and I. Tanaka, First principles phonon calculations in materials science, Scr. Mater. **108**, 1 (2015).

[32] K. Parlinski, Z. Q. Li, and Y. Kawazoe, First-Principles Determination of the Soft Mode in Cubic ZrO_2, Phys. Rev. Lett. **78**, 4063 (1997).

[33] L. Bjerg, G. K. H. Madsen, and B. B. Iversen, Enhanced thermoelectric properties in zinc antimonides, Chem. Mater. **23**, 3907 (2011).

[34] K. Persson, Materials data on VZn_3 (SG:221) by Materials Project, http://www.osti.gov/servlets/purl/1188083 (2014).

[35] K. Persson, Materials data on V_4Zn_5 (SG:139) by Materials Project, http://www.osti.gov/servlets/purl/1205236 (2016).

[36] K. Persson, Materials data on VSb (SG:194) by Materials Project, http://www.osti.gov/servlets/purl/1307625 (2016).

[37] K. Persson, Materials data on VSb_2 (SG:140) by Materials Project, http://www.osti.gov/servlets/purl/1202602 (2016).

[38] K. Persson, Materials data on V_3Sb_2 (SG:166) by Materials Project, http://www.osti.gov/servlets/purl/1204062 (2016).

[39] K. Persson, Materials data on V_5Sb_4 (SG:87) by Materials Project, http://www.osti.gov/servlets/purl/1204935 (2016).

[40] K. Persson, Materials data on V_3Sb (SG:223) by Materials Project, http://www.osti.gov/servlets/purl/1191232 (2015).

[41] W. B. Pearson, The Cu_2Sb and related structures, Z. Kristallogr. **171**, 23 (1985).

[42] G. Street, The magnetic properties of the manganese-gallium-aluminum-germanium system, J. Solid State Chem. **7**, 316 (1973).

[43] J. B. Goodenough, *Magnetism and Chemical Bond* (Interscience Publishers (Wiley), New York, 1963).

[44] D. Rogers, J. Gillson, and T. Gier, Hydrothermal crystal growth and electrical conductivity of the spinel LiV_2O_4, Solid State Commun. **5**, 263 (1967).

[45] G. K. White, Thermal expansion of magnetic metals at low temperatures, Proc. Phys. Soc. **86**, 159 (1965).

[46] S. Lutfalla, V. Shapovalov, and A. T. Bell, Calibration of the DFT/GGA+U method for determination of reduction energies for transition and rare earth metal oxides of Ti, V, Mo, and Ce, J. Chem. Theory Comput. **7**, 2218 (2011).

[47] C. Weber, D. D. O'Regan, N. D. M. Hine, M. C. Payne, G. Kotliar, and P. B. Littlewood, Vanadium Dioxide: A Peierls-Mott Insulator Stable Against Disorder, Phys. Rev. Lett. **108**, 256402 (2012).

[48] E. Goh, J. Mah, and T. Yoon, Effects of Hubbard term correction on the structural parameters and electronic properties of wurtzite ZnO, Comput. Mater. Sci. **138**, 111 (2017).

[49] M. B. Kanoun, S. Goumri-Said, U. Schwingenschlögl, and A. Manchon, Magnetism in Sc-doped ZnO with zinc vacancies: A hybrid density functional and GGA+U approaches, Chem. Phys. Lett. **532**, 96 (2012).

[50] A. D. Vries and C. Haas, Magnetic susceptibility and nuclear magnetic resonance of vanadium sulfides, J. Phys. Chem. Solids **34**, 651 (1973).

[51] J. B. Goodenough, Anomalous properties of the vanadium oxides, Annu. Rev. Mater. Sci. **1**, 101 (1971).

[52] B. Chamberland and T. Hewston, Co-existence of localized and itinerant electrons in the LiV_2O_4 system, Solid State Commun. **58**, 693 (1986).

[53] J. R. Anderson, G. Kido, Y. Nishina, M. Gorska, L. Kowalczyk, and Z. Golacki, Influence of pair-exchange interaction on the magnetization of IV-VI-compound diluted magnetic semiconductors, Phys. Rev. B **41**, 1014 (1990).

[54] C.-J. Chen, W. Gao, Z.-F. Qin, W. Hu, M. Qu, and W. Giriat, Magnetization and magnetic susceptibility of the diluted magnetic semiconductors $Zn_{1-x}Co_xS$ and $Zn_{1-x}Co_xSe$, J. Appl. Phys. **70**, 6277 (1991).

[55] F. W. Smith, Magnetization of a dilute magnetic alloy with magnetic interactions: ZnMn, Phys. Rev. B **10**, 2980 (1974).

[56] J. M. Franz and D. M. Sellmyer, Magnetic interactions and high-field magnetization in dilute magnetic alloys, Phys. Rev. B **8**, 2083 (1973).

[57] M. Imai, T. Naka, T. Furubayashi, H. Abe, T. Nakama, and K. Yagasaki, Electrical properties of polycrystalline $SrSi_2$, Appl. Phys. Lett. **86**, 032102 (2005).

[58] H. Nakamura, K. Ito, and M. Shiga, Semimetallic behaviour of $YInCu_4$ and $LuInCu_4$, J. Phys.: Cond. Matter **6**, 9201 (1994).

[59] J. H. Mooij, Electrical conduction in concentrated disordered transition metal alloys, Phys. Status Solidi A **17**, 521 (1973).

[60] T. Fukuda, T. Kakeshita, T. Saburi, K. Kindo, T. Takeuchi, M. Honda, and Y. Miyako, Negative temperature dependence of electrical resistivity in Ti-Ni alloys, Physica B **237–238**, 609 (1997).

[61] G. Reiss, J. Vancea, and H. Hoffmann, Grain-Boundary Resistance in Polycrystalline Metals, Phys. Rev. Lett. **56**, 2100 (1986).

[62] J. Tyan and J. T. Lue, Grain boundary scattering in the normal state resistivity of superconducting NbN thin films, J. Appl. Phys. **75**, 325 (1994).

[63] J. F. Moulder, W. F. Stickle, P. E. Sobol, and K. D. Bomben, in *Handbook of X-Ray Photoelectron Spectroscopy*, edited by J. Chastain (Perkin-Elmer Corporation, Minnesota, USA, 1995), pp. 230–232.

[64] E. Hryha, E. Rutqvist, and L. Nyborg, Stoichiometric vanadium oxides studied by XPS, Surf. Interf. Anal. **44**, 1022 (2012).

[65] G. Silversmit, D. Depla, H. Poelman, G. B. Marin, and R. D. Gryse, Determination of the V2p XPS binding energies for different vanadium oxidation states (V^{5+} to V^{0+}), J. Electron. Spectrosc. Relat. Phenom. **135**, 167 (2004).

[66] G. A. Sawatzky and D. Post, X-ray photoelectron and Auger spectroscopy study of some vanadium oxides, Phys. Rev. B **20**, 1546 (1979).

[67] F. M. F. de Groot, J. C. Fuggle, B. T. Thole, and G. A. Sawatzky, 2p x-ray absorption of 3d transition-metal compounds: An atomic multiplet description including the crystal field, Phys. Rev. B **42**, 5459 (1990).

[68] H. F. Pen, L. H. Tjeng, E. Pellegrin, F. M. F. De Groot, G. A. Sawatzky, M. A. van Veenendaal, and C. T. Chen, Phase transition in $LiVO_2$ studied by near-edge x-ray-absorption spectroscopy, Phys. Rev. B **55**, 15500 (1997).

[69] J.-H. Park, L. H. Tjeng, A. Tanaka, J. W. Allen, C. T. Chen, P. Metcalf, J. M. Honig, F. M. F. de Groot, and G. A. Sawatzky, Spin and orbital occupation and phase transitions in V_2O_3, Phys. Rev. B **61**, 11506 (2000).

[70] M. W. Haverkort, Z. Hu, A. Tanaka, W. Reichelt, S. V. Streltsov, M. A. Korotin, V. I. Anisimov, H. H. Hsieh, H.-J. Lin, C. T. Chen *et al.*, Orbital-Assisted Metal-Insulator Transition in VO_2, Phys. Rev. Lett. **95**, 196404 (2005).

[71] Z. Hiroi, S. Yonezawa, Y. Nagao, and J. Yamaura, Extremely strong-coupling superconductivity and anomalous lattice properties in the β-pyrochlore oxide KOs_2O_6, Phys. Rev. B **76**, 014523 (2007).

[72] L. Xie, T. Su, and X. Li, Magnetic field dependence of Schottky anomaly in the specific heats of stripe-ordered superconductors $La_{1.6-x}Nd_{0.4}Sr_xCuO_4$, Physica C **480**, 14 (2012).

[73] S. Yadam, D. Singh, D. Venkateshwarlu, M. K. Gangrade, S. S. Samatham, and V. Ganesan, Magneto-heat capacity study on Kondo lattice system $Ce(Ni_{1-x}Cu_x)_2Al_3$, Bull. Mater. Sci. **39**, 537 (2016).

[74] E. M. Brüning, C. Krellner, M. Baenitz, A. Jesche, F. Steglich, and C. Geibel, CeFePO: A Heavy Fermion Metal with Ferromagnetic Correlations, Phys. Rev. Lett. **101**, 117206 (2008).

[75] J.-X. Zhu, M. Janoschek, D. S. Chaves, J. C. Cezar, T. Durakiewicz, F. Ronning, Y. Sassa, M. Mansson, B. L. Scott, N. Wakeham *et al.*, Electronic correlation and magnetism in the ferromagnetic metal Fe_3GeTe_2, Phys. Rev. B **93**, 144404 (2016).

[76] J. Chen, Z. Wang, S. Zheng, C. Feng, J. Dai, and Z. Xu, Antiferromagnetic Kondo lattice compound $CePt_3P$, Sci. Rep. **7**, 41853 (2017).

[77] D. W. Cooke, Z. Boekelheide, D. R. Queen, and F. Hellman, The role of the spin-density wave and disorder in the density of states of sputtered Cr films, J. Appl. Phys. **105**, 07C314 (2009).

[78] K. Gschneidner, J. Tang, S. Dhar, and A. Goldman, False heavy fermions, Physica B **163**, 507 (1990).

[79] E. Svanidze, A. Amon, Y. Prots, A. Leithe-Jasper, and Y. Grin, Abnormal specific heat enhancement and non-Fermi-liquid behavior in the heavy-fermion system $U_2Cu_{17-x}Ga_x(5 \leqslant x \leqslant 8)$, Phys. Rev. B **97**, 115148 (2018).

[80] A. Krimmel, M. Reehuis, and A. Loidl, CF effects and disorder versus Kondo lattice behavior in $CeTSi_3$ (T = Rh, Ir), Appl. Phys. A **74**, s695 (2002).

[81] P. Zalden, K. S. Siegert, S. Rols, H. E. Fischer, F. Schlich, T. Hu, and M. Wuttig, Specific heat of $(GeTe)_x(Sb_2Te_3)_{1-x}$ phase-change materials: The impact of disorder and anharmonicity, Chem. Mater. **26**, 2307 (2014).

[82] C. A. Martin, Simple treatment of anharmonic effects on the specific heat, J. Phys. Cond. Matter. **3**, 5967 (1991).

[83] W. Schweika, R. P. Hermann, M. Prager, J. Persson, and V. Keppens, Dumbbell Rattling in Thermoelectric Zinc Antimony, Phys. Rev. Lett. **99**, 125501 (2007).

[84] M. J. Winiarski and T. Klimczuk, Crystal structure and low-energy Einstein mode in ErV_2Al_{20} intermetallic cage compound, J. Solid State Chem. **245**, 10 (2017).

[85] Y. Li, H. Y. Bai, W. H. Wang, and K. Samwer, Low-temperature specific-heat anomalies associated with the boson peak in CuZr-based bulk metallic glasses, Phys. Rev. B **74**, 052201 (2006).

[86] V. Lubchenko and P. G. Wolynes, The origin of the boson peak and thermal conductivity plateau in low-temperature glasses, Proc. Natl. Acad. Sci. USA **100**, 1515 (2003).

[87] A. I. Chumakov, G. Monaco, A. Monaco, W. A. Crichton, A. Bosak, R. Rüffer, A. Meyer, F. Kargl, L. Comez, D. Fioretto *et al.*, Equivalence of the Boson Peak in Glasses to the Transverse Acoustic Van Hove Singularity in Crystals, Phys. Rev. Lett. **106**, 225501 (2011).

[88] S. N. Taraskin, Y. L. Loh, G. Natarajan, and S. R. Elliott, Origin of the Boson Peak in Systems with Lattice Disorder, Phys. Rev. Lett. **86**, 1255 (2001).

[89] E. Liang, Y. Liang, Y. Zhao, J. Liu, and Y. Jiang, Low-frequency phonon modes and negative thermal expansion in $A(MO_4)_2$ (A = Zr, Hf and M = W, Mo) by Raman and Terahertz time-domain spectroscopy, J. Phys. Chem. A **112**, 12582 (2008).

[90] P. Svoboda, P. Javorský, M. Diviš, V. Sechovský, F. Honda, G. Oomi, and A. A. Menovsky, Importance of anharmonic terms in the analysis of the specific heat of UNi_2Si_2, Phys. Rev. B **63**, 212408 (2001).

[91] K. Procházková, S. Danis, and P. Svoboda, Specific heat study of $PrNi_4Si$, Acta Phys. Pol. A **113**, 299 (2008).

[92] J. Garg, N. Bonini, B. Kozinsky, and N. Marzari, Role of Disorder and Anharmonicity in the Thermal Conductivity of Silicon-Germanium Alloys: A First-Principles Study, Phys. Rev. Lett. **106**, 045901 (2011).

[93] A. Fujimori, Electronic structure of metallic oxides: Band-gap closure and valence control, J. Phys. Chem. Solids **53**, 1595 (1992).

[94] J. B. Torrance, P. Lacorre, A. I. Nazzal, E. J. Ansaldo, and C. Niedermayer, Systematic study of insulator-metal transitions in perovskites $RNiO_3$ (R = Pr, Nd, Sm, Eu) due to closing of charge-transfer gap, Phys. Rev. B **45**, 8209 (1992).

[95] P. Lacorre, J. Torrance, J. Pannetier, A. Nazzal, P. Wang, and T. Huang, Synthesis, crystal structure, and properties of metallic $PrNiO_3$: Comparison with metallic $NdNiO_3$ and semiconducting $SmNiO_3$, J. Solid State Chem. **91**, 225 (1991).

[96] J. L. García-Muñoz, M. Suaaidi, M. J. Martínez-Lope, and J. A. Alonso, Influence of carrier injection on the

metal-insulator transition in electron- and hole-doped $R_{1-x}A_xNiO_3$ perovskites, Phys. Rev. B **52**, 13563 (1995).

[97] X. Obradors, L. M. Paulius, M. B. Maple, J. B. Torrance, A. I. Nazzal, J. Fontcuberta, and X. Granados, Pressure dependence of the metal-insulator transition in the charge-transfer oxides $RNiO_3$ (R = Pr, Nd, $Nd_{0.7}La_{0.3}$), Phys. Rev. B **47**, 12353 (1993).

[98] C. Grygiel, A. Pautrat, W. Prellier, and B. Mercey, Hysteresis in the electronic transport of V_2O_3 thin films: Non-exponential kinetics and range scale of phase coexistence, Europhys. Lett. **84**, 47003 (2008).

[99] A. Dvurečenskij, P. Billik, A. Cigáň, R. Bystrický, J. Maňka, M. Škrátek, and M. Majerová, Magnetic properties of V_2O_3 nanooxide prepared mechanochemically with and without salt matrix, Acta Phys. Pol. A **126**, 398 (2014).

[100] A. E. Bocquet, T. Mizokawa, K. Morikawa, A. Fujimori, S. R. Barman, K. Maiti, D. D. Sarma, Y. Tokura, and M. Onoda, Electronic structure of early 3d-transition-metal oxides by analysis of the 2p core-level photoemission spectra, Phys. Rev. B **53**, 1161 (1996).

[101] T. Uozumi, K. Okada, A. Kotani, R. Zimmermann, P. Steiner, S. Hüfner, Y. Tezuka, and S. Shin, Theoretical and experimental studies on the electronic structure of M_2O_3 (M = Ti, V, Cr, Mn, Fe) compounds by systematic analysis of high-energy spectroscopy, J. Electron. Spectrosc. Relat. Phenom. **83**, 9 (1997).